ACS APPLIED MATERIALS & INTERFACES
Research Article
Cite This: ACS Appl. Mater. Interfaces 2018, 10, 3011−3019
www.acsami.org

Atomic Origins of the Self-Healing Function in Cement−Polymer Composites

Manh-Thuong Nguyen,[†] Zheming Wang,[§] Kenton A. Rod,[‡] M. Ian Childers,[‡] Carlos Fernandez,[*,‡] Phillip K. Koech,[‡] Wendy D. Bennett,[‡] Roger Rousseau,[†] and Vassiliki-Alexandra Glezakou[*,†]

[†]Basic and Applied Molecular Foundations, Physical and Computational Sciences Directorate, [‡]Energy and Environment Directorate, and [§]Geochemistry, Physical and Computational Sciences Directorate, Pacific Northwest National Laboratory, P.O. Box 999, Richland, Washington 99352, United States

Supporting Information

ABSTRACT: Motivated by recent advances in self-healing cement and epoxy polymer composites, we present a combined ab initio molecular dynamics and sum frequency generation (SFG) vibrational spectroscopy study of a calcium−silicate−hydrate/polymer interface. On stable, low-defect surfaces, the polymer only weakly adheres through coordination and hydrogen bonding interactions and can be easily mobilized toward defected surfaces. Conversely, on fractured surfaces, the polymer strongly anchors through ionic Ca−O bonds resulting from the deprotonation of polymer hydroxyl groups. In addition, polymer S−S groups are turned away from the cement−polymer interface, allowing for the self-healing function within the polymer. The overall elasticity and healing properties of these composites stem from a flexible hydrogen bonding network that can readily adapt to surface morphology. The theoretical vibrational signals associated with the proposed cement−polymer interfacial chemistry were confirmed experimentally by SFG vibrational spectroscopy.

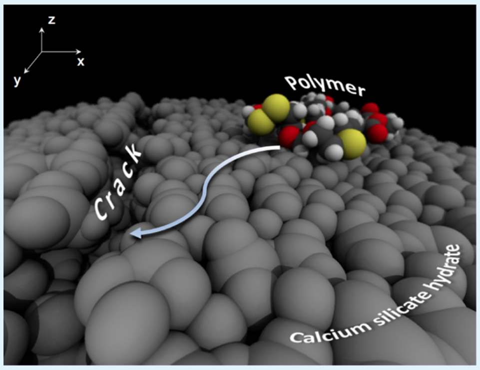

KEYWORDS: *self-healing cement, C−S−H model, SFG, ab initio molecular simulations, geothermal, well-bore cement*

INTRODUCTION

As a fundamental infrastructure material, cement has been, in terms of mass, one of the most used materials in the world, with calcium−silicate−hydrate (C−S−H) being its main component. Incorporation of chemical additives to improve cement durability is a centuries-old practice,[1−3] and modern theory and characterization techniques can now be used to access structural information in complicated media such as cementitious materials.[4] Understanding its properties to improve its performance in practical applications summons endless efforts in the materials research community.[5−7] The addition of small amounts of polymers to C−S−H has been shown to reinforce and improve mechanical properties such as tensile strength of C−S−H.[8−10] What is known about polymer/C−S−H composites has been acquired from various preparation and characterization studies.[8−11] Depending on the experimental conditions and/or the chemical nature of polymers and C−S−H, their composites can be prepared through intercalation,[8] exfoliation,[11,12] or direct chemical (covalent) bonding.[13] As an example, to synthesize the covalent composites of polymers and C−S−H, the polymers contain silane functions that are incorporated into the silicate chains of C−S−H.[13] These findings are based on experimental techniques, such as nuclear magnetic resonance spectroscopy or X-ray powder diffraction. However, because of the structural complexity and diversity, nanostructures and local chemical properties of polymer/C−S−H composites are rather challenging to determine. In addition, there is no straightforward way of predicting the best polymer/C−S−H formulations with specific functionalities. To achieve that, computational modeling can help identify the key molecular structure parameters that relate to specific macroscopic properties.

There is a fair number of computational studies based on classical molecular dynamics or Monte Carlo approaches that have contributed to a better understanding of the link between the molecular structure and the mechanical properties of C−S−H.[5,6,14] Shalchy and Rahbar have investigated interfaces of C−S−H and nylon-6, poly(vinyl)alcohol (PVA), and polypropylene using atomistic simulations.[15] They found that the adhesion energy increases against the calcium−silicate ratio, with nylon-6 appearing more adhesive than PVA and polypropylene. These authors showed that the electrostatic and van der Waals interactions mainly contribute to the total adhesion energies, while hydrogen bonding is almost negligible. Conversely, Sakhavand and co-workers in another computational study highlighted the importance of hydrogen bonding to PVA−tobermorite interactions.[16] This implies that theoretical approaches can significantly shape our understanding of these composites at the atomistic level. More importantly, to understand local chemical transformation processes at poly-

Received: September 2, 2017
Accepted: December 29, 2017
Published: December 29, 2017

DOI: 10.1021/acsami.7b13309

mer/C−S−H interfaces, a quantum mechanical approach is essential, such that both covalent and hydrogen bonding can be assessed on the same footing and connect the molecular structure to properties.

A highly practical and important use of cement−polymer composites is to upgrade the functions of cement used in wellbores. The sealing of wellbores used for oil, gas, and geothermal heat production is a major environmental matter. Primary cementing completes this crucial task by filling the annulus between the geological formation and wellbore casing with cement.[17] The failure of the cement lining of the geothermal wells caused by the high temperature (up to 400 °C) and chemically corrosive geothermal production environments always lead to very bad environmental and economic impacts. There have been considerable attempts to tackle these problems; however, despite advancement in the development of cementitious materials for geothermal applications and self-healing cements in general,[18,19] self-healing cements with improved adhesion at both the casing and formation interfaces under geothermal conditions have only recently been developed by us.[20] We have carried out a systematic study suggesting that the addition of select polymers, such as self-healable thermoset epoxy resins, into cements can produce a composite with self-healing and readhering abilities.[20] This novel polymer−cement composite possesses various desirable properties such as high stability at most geothermal temperatures, self-healing ability, or sealing fractures with wide apertures, and constitutes a much-improved alternative to conventional wellbore cement materials. Motivated by these findings as well as the need to connect molecular-level information with macroscopic properties to enable a predictive design, we performed ab intio molecular dynamics (AIMD) that explicitly account for the roles of electrons and nuclei at finite temperatures. We present a range of properties of polymer/C−S−H complexes derived from AIMD, and to our knowledge, this is a first study of its kind for these materials. The results reveal the following: (i) hydrogen bonding between polymer and C−S−H oxygen atoms, (ii) ionic bonding between the polymer oxygen and C−S−H calcium species, and (iii) van der Waals interactions. More importantly, the simulations also show proton transfer from pendant OH groups of the polymer, demonstrating that OH groups are crucial in enhancing the polymer/C−S−H adhesion. Our simulations show that O−Si bond formation between the polymer and C−S−H is not likely, as unsaturated Si atoms were found to be hydrolyzed by additional water molecules. Validation of these findings was obtained by sum frequency generation (SFG) spectroscopic (SFG-VS) studies. The remarkable agreement between the predicted polymer−cement interactions responsible for the material's properties and the corresponding experimental vibrational signatures associated to these interactions demonstrate the potential of AIMD methods for the predictive design.

■ METHODS

AIMD Simulations. All calculations were performed at the DFT level of theory by using the generalized gradient approximation with the Perdew−Burke−Ernzerhof[21−23] exchange correlation functional as implemented in the CP2K code.[24] Long-range and dispersion interactions were included through van der Waals correction D2, as proposed by Grimme.[25] We employed the Gaussian plane-wave hybrid basis set scheme[26] with the molecularly optimized double-ζ Gaussian basis sets[27] used to expand Kohn−Sham orbitals and a plane-wave expansion of the charge density with a 400 Ry cutoff. The norm-conserving pseudo-potentials GTH[28] were employed to describe the core electrons: [1s] for C, and O; [1s, 2s2p] for S, Si, and Ca. Brillouin zone sampling was performed by the Γ-point approximation.

MD simulations were performed within the canonical (NVT) ensemble at $T = 300$ K. To integrate the equation of motions, we adopted the Verlet integration scheme,[29] with the time step set at 0.55 fs. The systems were first equilibrated for at least 15 ps, followed by more than 25 ps of production runs.

Because of the computational cost of density-functional-based MD, a truncated model was used with a unit cell consisting of 902 atoms, formulated as $Ca_{124}Si_{80}O_{284}\cdot 138H_2O$. It has been shown that the local Ca/Si ratio varies from 0.6 to 2.3,[30] and in our model, this ratio is 1.55, which is very similar to the one used in the original material, 1.67,[31] and close to the realistic average value of 1.7.[32] The ratio of 1.55 implies that the molecular model used in the present study belongs to the γ class of C−S−H, as suggested by Nonat,[33] and it is similar in composition to others adopted in the the literature.[34] As shown in Figure S1a, the unit cell includes two layers of the same composition along the Z direction. We considered surfaces perpendicular to the X or Z direction (referred to as X-cut or Z-cut surfaces). While the Z-cut surface is a natural choice for layered or cured materials, the X-cut surface constitutes a representation of a surface induced by a mechanical crack. For the X-cut surface, the number of H and O atoms (in the form of broken H_2O molecules) was adjusted to maintain the stoichiometry. A truncated version of the polymer of interest is shown in Figure S1b. For the analysis purpose (section S3), we label parts of the polymer as: COC (epoxy groups), CO (carbonyl groups), OH (the hydroxyl groups), and backbone. The polymer was initially placed on the cement surface with its backbone nearly parallel to the surface to maximize the contact area. To study the effects of water on C−S−H/polymer bonding, 100 water molecules were added to the interface. Additional details about our theoretical approaches can be found in section S1−S5, Supporting Information.

Experiments. *Cement Synthesis.* Cement samples were synthesized by mixing the class H cement powder and silica flour in a poly(propylene) beaker, and then adding DI H_2O and mixing to give a cement slurry. The slurry was transferred to plastic molds and cured at 85 °C for 5 d at 99+% relative humidity. The mass ratios, water content, and curing temperature were selected to form tobermorite as the main mineral phase after the cement was cured.[17] Tobermorite is the mineral phase employed on the atomistic simulations. The cement samples were cut into hockey puck samples 0.5 cm thick, and the flat area of the samples was ground with 600 and 1200 grit silicon carbide papers.

Polymer Deposition on Cement Surfaces. Polymer samples were synthesized by mixing the monomers [9.6 g Thioplast 25, 9.6 g poly(ethylene glycol)diglycidyl ether, 6.5 g pentaerythritol tetrakis(3-mercaptopropionate)] and adding 1 wt % 4-dimethylaminopyridine (0.2 g) as a catalyst followed by remixing to give a homogeneous solution. The samples were spin-coated on the hockey puck-shaped cement samples, and the polymer-coated cement samples were cured for 2 h at 60 °C in a temperature-controlled oven.

SFG-VS Analysis. This technique is used to provide a qualitative picture of the interactions taking place at the interface of the cement and the polymeric coating. Because of the thickness of our polymer layer (27−30 μm), there was no special fitting of the data;[35−37] however, the results are presented as difference spectra, with the cement/air interface as a reference, to minimize the polymer/air interface contributions. SFG-VS spectra were collected in the range of 1200−4000 cm^{-1}. For additional details on the experimental work, please refer to section S6, Supporting Information.

■ RESULTS AND DISCUSSION

The surface models used in the simulations were adopted from a tobermorite-derived C−S−H structure proposed in a recent paper by Kovačević et al. (model 1).[31] Two surface terminations were considered along the X (X-cut) and Z (Z-cut) directions to simulate a cracked and a pristine cement surface, respectively; see Figure 1a,b of C−S−H. Our choice of

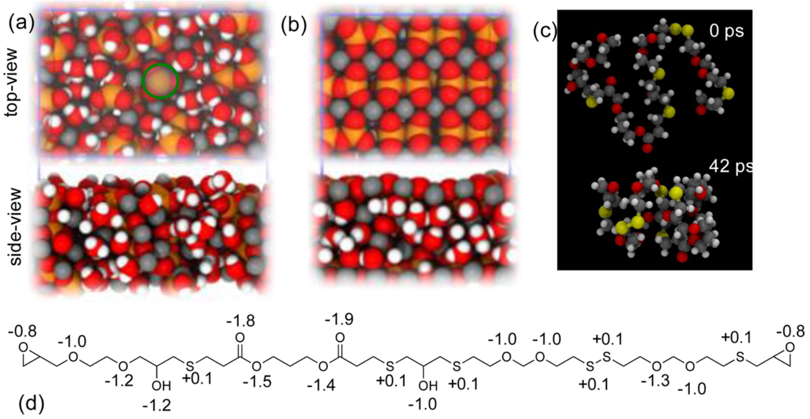

Figure 1. Top-view and side-view of (a) *X*-cut and (b) *Z*-cut of CSH surfaces, the circle indicates an undercoordinated Si atom (H white, O red, Ca gray, Si orange). (c) Polymer at 0 and 42 ps in the gas phase, (C in gray, O in red, S in yellow, H in white). (d) Bader charges of the polymer were estimated from the geometry at 42 ps.

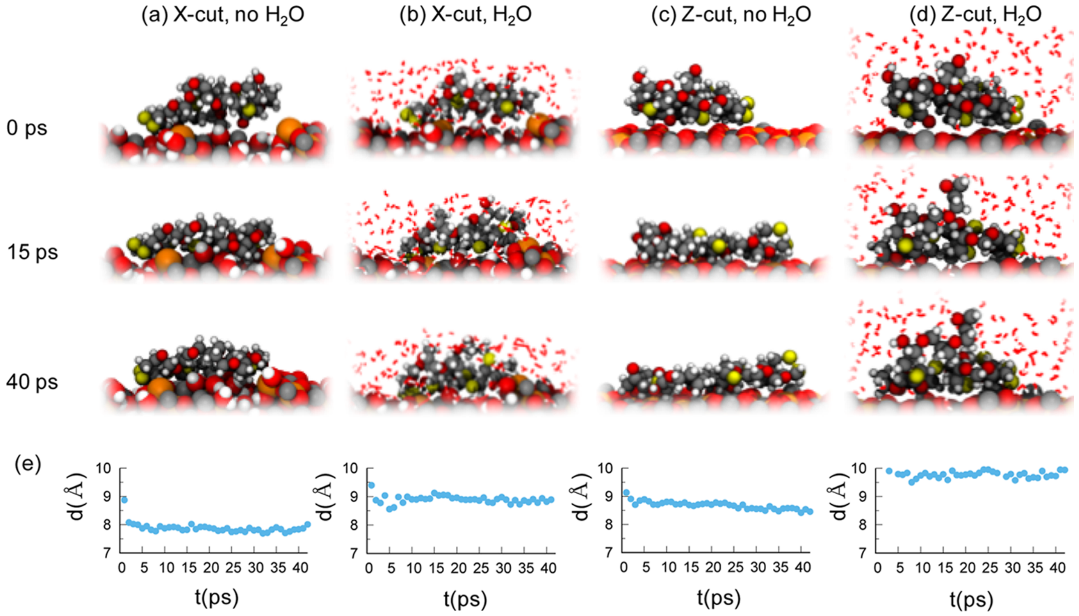

Figure 2. Geometry of the polymer at different times and averaged height of C atoms with respect to the center of the slab in the case of the *X*-cut surface (a) without water and (b) with water and the *Z*-cut surface (c) without water and (d) with water.

surface terminations was justified by nanoparticle structural studies as identified by means of computer simulations and scanning electron microscopy.[38,39]

Because of the high complexity of the material, the local chemical makeup of the two surfaces is quite diverse. After relaxation, the *X*-cut surface exposes an undercoordinated Si atom, marked with a circle in Figure 1a, while most of the surface area exposes Ca^{2+} species, and the surface termination appears to be highly disordered. As a result, water molecules saturated the low-coordination Si sites (in our case, only one such site exists in the simulation cell), creating hydroxyl groups, that further contribute to local disorder. We note that the undercoordinated Si atoms could potentially result from breaking of silicate chains if a crack occurs under extreme conditions such as those present in geothermal wellbores. Broken silicate chains in C−S−H have been reported in the literature.[40,41] We estimate the density of these species as $N_i/2A$, where $2A$ is the surface area in each unit cell in the slab model, resulting in surface densities of 0.004, 0.033, 0.028, 0.052, and 0.013 $Å^{-2}$ for Si, Ca, OH, O, and H_2O, respectively. Along the *Z* direction, the chemical makeup of the material is very different and more ordered. On the basis of other studies,[42] Ca^{2+} layers of C−S−H (*Z*-cut) and water appear to be stable structures; see Figure 1b. Our study also confirms these findings for the *Z*-cut surface, where we see primarily Ca−O interactions with a surface density of O and Ca at 0.100 and 0.048 $Å^{-2}$, respectively, and no other significant interatomic interactions.

To study the cement−polymer interface, a simplified polymer strand was used based on the polymer materials used in our recent study.[43]

The polymer with self-healing properties is decorated with several polarized functional groups (epoxy, hydroxyl, and carbonyl) that are more reactive than the backbone component CH, Figure 1c. Figure 1c shows the drastic change in the polymer conformation in the gas phase. A Bader analysis shows that the charge states of O atoms decrease in the following order: carbonyl O > O > hydroxyl O > epoxy O; see Figure 1d. The S atoms remain positively charged in all cases.

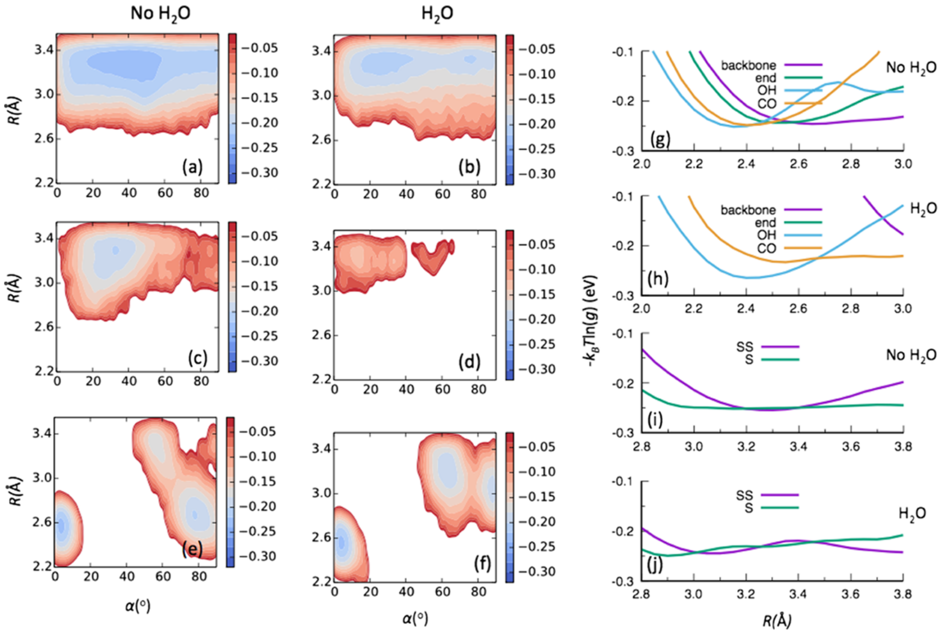

Figure 3. PMF (in eV) of the polymer on *X*-cut surfaces: (a,b) H bond with the C backbone, (c,d) H bond with C ends, (e,f) H bond with O hydroxyls, (g,h) Ca−O bonds with different O atoms, and (i,j) Ca−S bond without/with H_2O.

Two limiting hydration states were considered (without and with explicit water molecules above the C−S−H surfaces) to examine the interfacial structure and polymer dynamics. In Figure 2, we show the structural evolution of the C−S−H/polymer interface at 0, 15, and 40 ps without/with water for *X*- (Figure 2a,b) and *Z*-cuts (Figure 2c,d). The initial geometries (at 0 ps) of the C−S−Hpolymer interface were obtained from static optimizations. The plots at the bottom of Figure 2a−d show the average height of the polymer taken from the middle of the C−S−H slab. This distance quickly relaxes during the initial 5 ps of simulation and varies very little after that. We observe that in the absence of water, the polymer wets the C−S−H surface and relaxes relative to its gas phase conformation (Figure 2c). In the presence of water, the polymer contracts, and its distance *d* increases by ∼1.0 Å regardless of the surface termination, implying that water reduces the wetting of C−S−H by the polymer. This will be discussed further in the following section.

In the following section, we will present analysis of the dynamic behavior of bonding interactions of the functional groups and the calculated spectroscopic signatures of these systems.

Potential of the Mean Force of Polymer/C−S−H Interactions. To characterize the number and the type of polymer/C−S−H interactions, we constructed a 2D potential of the mean force (PMF) for the hydrogen bond DH···A between donor D and acceptor A using the geometrical criteria described by Kumar et al.[44] Here, the DA distance *r* and ∠HAD angle *α* are selected as parameters of the potential described by the equation

$$W(r,\alpha) = -k_BT\ \ln g(r,\alpha)$$

where k_B is the Boltzmann constant, T is the temperature, which was chosen to be 300 K for this study, and $g(r, \alpha)$ is the distribution function describing the probability of finding A and D at distance r and the three atoms H, A, and D forming an angle α. In a similar way, we can also characterize the dynamics of O−Ca and S−Ca bonds by choosing their interatomic distance as the reaction coordinates. A complementary analysis based on time correlation functions is presented in section S2 and Figures S3, and S4.

X-Cut. Surprisingly, we do not observe Si−O polymer interactions on the undercoordinated Si site of the *X*-cut surface. In the case where there is no water, we do not anticipate any effect of these defects on the binding pattern between the cement and the polymer, and we attribute this to the above-mentioned low surface density of Si sites and possibly the short AIMD time. However, in the presence of water, these Si sites become readily populated by water molecules, which dissociate into silanols and protons bound to surface oxygens. This underscores the point that water, which is ubiquitous in these composites, is expected to passivate the unsaturated Si sites owing to strong Si−O bonds.

In Figure 3a−f, we show the PMF of hydrogen bonds formed between C−S−H O atoms of the *X*-cut substrate and polymer (−O, C)H atoms. In each PMF, one, two, or three lowest energy basins are clearly identified. In Figure 3a, the lowest energy basin for the polymer backbone and C−S−H H bonds are most clearly described by the distance of 3.1−3.4 Å and angle 15°−55°. In the presence of water, the H bonds associated with the backbone of the polymer become a shallower, bimodal distribution in the PMF, as shown in Figure 3b. This is consistent with the longer distance of the polymer from the surface and increased flexibility to maximize favorable interactions in the presence of water.

The H-bond associated with the epoxy groups has structural parameters similar to those of the backbone, as shown in Figure 3c,d. However, the epoxy H-bonds have a narrower *α* range, which can be attributed to the flexibility of the epoxy groups being at two ends of the polymer. In the presence of water, these interactions become markedly weaker because of the high affinity of the epoxy groups to the water that almost eliminates their interaction with the surface.

The hydrogen bonding with the hydroxyl groups is the most dynamic feature, as shown in Figure 3e,f. On the left of the PMF surface, a deep basin arises from the dissociation of a

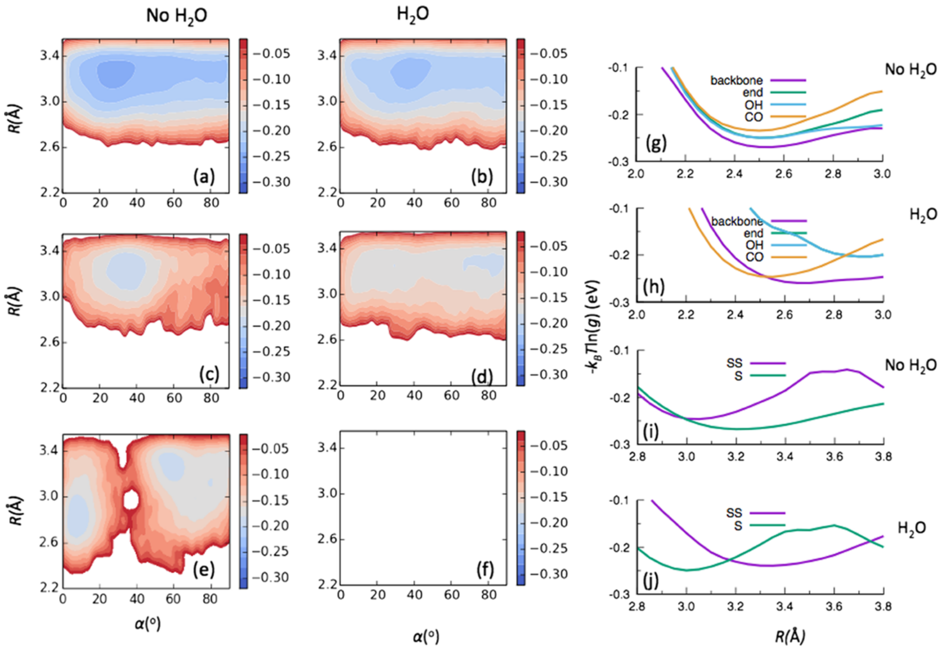

Figure 4. PMF of the polymer on Z-cut surfaces: (a,b) H bond with a C backbone, (c,d) H bond with C ends, (e,f) H bond with O hydroxyls, (g,h) Ca−O bonds with different O atoms, (i,j) Ca−S bond without and with H_2O.

hydroxyl group of the polymer, creating a new one on the cement's surface, (C−S−H)O···HO(polymer) → (C−S−H)OH···O(polymer). With α being less than 10°, three atoms O(C−S−H), H(polymer), and O(polymer) are almost on a straight line. Furthermore, the O−O distance is ∼2.5 Å with a resulting H-acceptor distance of ∼1.6 Å, indicating a strong H-bond. In the presence of water, this peak remains, while the ones associated with larger angle contacts are shifted.

We now analyze the Ca−O(polymer) bonds. Figure 3g (blue line) shows that the shortest Ca−O(polymer) bond length is the bond length between the O atom of a dissociated hydroxyl group (alkoxide) and a Ca surface atom, which is ∼2.35 Å. These interactions are strong enough to remain essentially unchanged in the presence of water, as shown in Figure 3h (blue line). The second shortest O−Ca bonds involve interactions with the polymer carbonyl groups, as shown in Figure 3g,h (yellow lines). In the absence of water, there is a broad yet well-defined minimum at ∼2.4 Å, while the presence of water significantly softens this interaction. This picture counters the charge distribution based on the gas phase polymer charges, where the carbonyls carry the most negative charge and as such would have been expected to foster the strongest interactions with the surface. This is a result of the dissociative chemistry of the hydroxyl groups that we are able to capture with the AIMD simulations and would have been otherwise missed.

The PMF for the Ca−S bond is shown in Figure 3i,j. In the absence of water, the bond lengths (∼3.3 Å) are relatively long and characterized by soft and broad wells, indicating rather weak interactions between S and Ca. These interactions essentially disappear in the presence of water. This is a reflection of the re-orientation of the polymer in the presence of water to expose the more hydrophilic groups such as the carbonyls to the water, rather than changing the actual chemical bonding to the surface.

It is known that polymers and C−S−H can be covalently bonded. This may be driven by the incorporation of the polymer's silane functions into the silicate chains of C−S−H.[13] Such a covalent link acts as an anchor binding the polymers and C−S−H together. In our systems, the covalent character is missing in the polymer/C−S−H bonding. Even in the X-cut surface case, undercoordinated Si atoms (which can be result from a crack) were quickly saturated with dissociated water or stayed intact during the simulations. A possibility of forming covalent bonds between the polymer and C−S−H is that the dissociated hydroxyl group (O^-) couples with the undercoordinated Si atom.

Z-Cut. Similar to the X-cut surface, in the absence of water, the H-bonds involving the polymer's backbone are more pronounced with an energy basin located at r = 3.1−3.4 Å and α = 15°−40°, as shown in Figure 4a,b. The H-bonds with the epoxy groups have a similar structural parameter range in the absence of water but exhibit a flatter potential, whose minimum shifts to wider angles in the presence of water, as shown in Figure 4c,d. This feature is very different than the X-cut, where water completely eliminates this interaction; see the Results and Discussion section.

There are two distinguishable energy basins in the case of the hydroxyl groups; however, we did not observe any OH dissociation within our simulation time length. The most profound change is observed in the presence of water, where these interactions are completely absent, as shown in Figure 4e,f.

For Ca−O bonds (Figure 4g,h) without water, all bond lengths correlate well with the charges of O atoms in the increasing order: CO > backbone > OH > epoxy. The shortest bond length is about 2.5 Å, which is consistent with a Ca−O ionic bond. The presence of water clearly weakens these interactions such that only Ca-carbonyl persists. The Ca−S interactions without water are stronger for the SS links and softer for the thio-ether, whereas the opposite is true with water. Nevertheless, with or without water, the Ca−S bonds are 3.0 Å or longer, indicating that these interactions are of a weak van der Waals type.

The abovementioned observations paint a completely different molecular binding of the polymer on the two surface cuts. On the more stable *Z*-cut, the interactions are largely weak hydrogen and coordination bonds, all of which weaken further or disappear in the presence of water. Conversely, the *X*-cut is conducive to stronger ionic interactions, resulting from reactions with the polymer hydroxyl groups with Ca of C−S−H. In section S2, we perform a time-dependent analysis of individual interactions that provides qualitative insights on the durability of intermolecular interactions related to short time polymer dynamics. While the PMF analysis gave a perspective view of the role of the OH groups in anchoring the polymer to the *X*-cut but not the *Z*-cut, this last analysis shows that some of these interactions can readily break and re-form, adding elasticity to the treated C−S−H surface.

Shape and Elasticity of the Polymer Fragment. To further examine the impact the binding to the C−S−H surface has on the polymer side chain, we examine the properties of the moment of the inertia tensor, *I*, whose eigenvalues (I_1, I_2, and I_3) can be used to describe the shape of the polymer fragment. The probability distribution function $P(I)$ of the eigenvalues for the gas phase, *X*-cut without/with water, and *Z*-cut without/with water are plotted in Figure 5. As a reference for the gas phase polymer $I_1 \approx I_2 \approx I_3$, Figure 5a indicates that the polymer is mostly uniformly distributed in space as a tightly packed ball in good accord with the representative structure in Figure 1c.

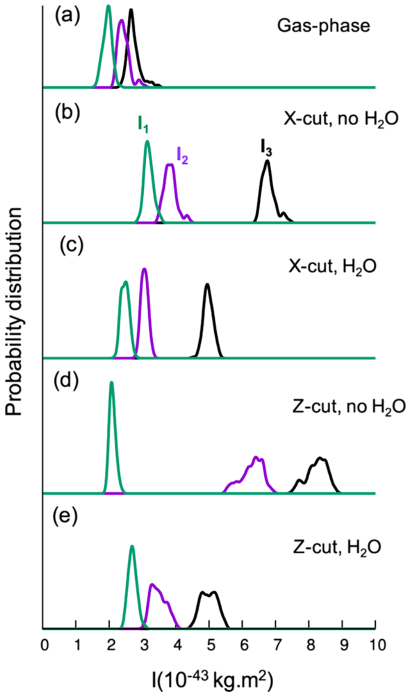

Figure 5. Probability distribution of the moments of inertia (I_k, $k = 1, 2, 3$) of the polymer: (a) gas phase; (b) *X*-cut without water; (c) *X*-cut with water; (d) *Z*-cut without water, and (e) *Z*-cut with water.

On the *X*-cut surface, all three moments of inertia increase in the size relative to those of the gas phase. Without water, $I_1 \approx I_2 < I_3$ indicates that the polymer has taken on an elongated cigar shape as it is adsorbed onto the *X*-cut. This shape is retained on the *X*-cut with or without water with the notable observation that all three eigenvalues decrease, particularly in the presence of water. In all cases, the distributions of each eigenvalue are approximately Gaussian in shape with a notable presence of small shoulders in the absence of water. The width of the Gaussian provides a measure of the flexibility or elasticity of the polymer which can be seen to be approximately 10% less in the presence of water owing to hydrophobic repulsion of the outside of the polymer with the surrounding water molecules. Hence, on the *X*-cut, water both compresses and tightens the polymer.

As can be inferred from Figure 2d,e, the impact of water on the polymer bound to the *Z*-cut is far more noticeable. Without water, the polymer is distributed as an elliptical pancake, $I_1 \ll I_2 < I_3$ on the surface (I_1 pointing along the surface normal). The width of the distribution of I_2 and I_3 is approximately twice that of the analogous moments on the *X*-cut, and the bimodal nature of each peak is distinctly pronounced. We can thus conclude that the polymer is far more flexible on the *Z*-cut than on the *X*-cut. Addition of water again caused the polymer to contract such that $I_1 \approx I_2 < I_3$, and the polymer takes on a shape which is similar to that on the *X*-cut with the notable exception that the width of $P(I)$ for I_2 and I_3 is twice as broad.

In a parallel analysis in section S3, we find that the center of mass of the polymer is able to oscillate more on the *X*-cut than on the *Z*-cut, suggesting a high mobility on the surface. In short, the strong anchoring of the polymer on the *X*-cut via cement−polymer Ca−O contacts leads to a rigid polymer surface interface that aids to the increase in rigidity. Conversely, on the more stable *Z*-cut, the polymer is more flexible and more mobile, and water acts as an agent to enhance mobility with only a slight impact on flexibility.

Electronic Properties. To provide more insights into the bonding picture of the polymer with the C−S−H surfaces, we now look at the bonding charge density difference in the system, which is given by

$$\Delta\rho = \rho(\mathrm{p/wCSH}) - \rho(\mathrm{p}) - \rho(\mathrm{wCSH})$$

where ρ is the electron density of the system(s) and p and w denote the polymer and water, respectively. In Figure 6, we show the electron density difference obtained for select configurations after ~50 ps of simulation time.

On the *X*-cut surfaces, we found a significant charge rearrangement at the polymer/C−S−H interface in the absence of water, as shown in Figure 6a. This is because of the dissociation of the polymer hydroxyl group, which is shown as charge accumulation near the polymer's H and O atoms at the interface with C−S−H. The presence of water, as shown in Figure 6b, does not change this picture but only slightly attenuates/screens this charge transfer. This is visible in the charge delocalization in the surrounding water molecules and solvated epoxy groups.

On the *Z*-cut surfaces, the charge rearrangement is appreciably smaller owing to the weaker contacts described above and can be attributed mostly to polarization of the polymers' functional groups in the immediate vicinity of the surface, as shown in Figure 6c. The presence of water increases the charge transfer due to the increased H bonding between the polymer and water molecules, as shown in Figure 6d. Because of the very limited C−S−H/polymer interactions, a more significant charge transfer to water molecules occurs away from the surface. This is a dramatic visualization of the competition between water and C−S−H for binding to the polymer. On the *X*-cut surface, because these interactions are strong, water in mostly excluded. However, on the *Z*-cut surface, polymer−water interactions dominate their partition: as a result, water

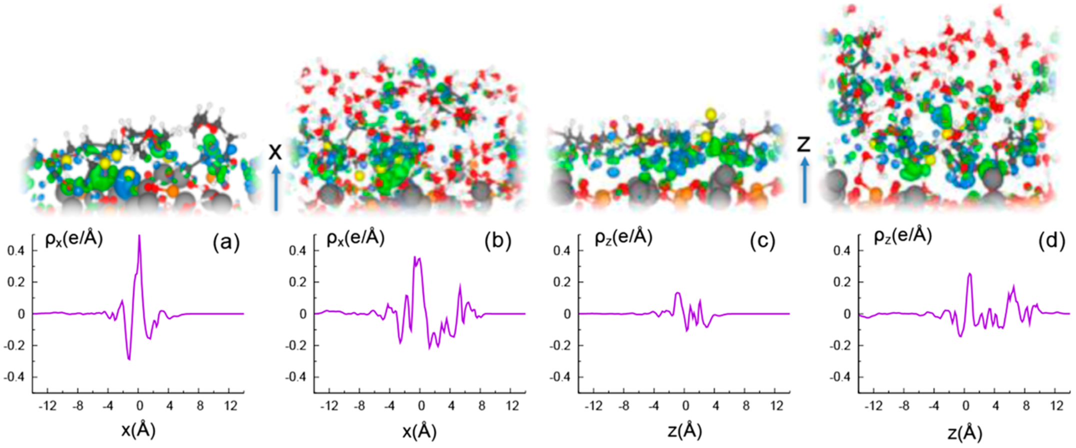

Figure 6. Bonding charge density of the polymer at the *X*-cut surfaces without (a) and with (b) water and at the *Z*-cut surfaces without (c) and with (d) water; isosurface value is set at 0.003 au, charge gain is represented in green, and charge loss is represented in blue. The bottom panels show the averaged bonding charge density with the interface plane position set at 0.

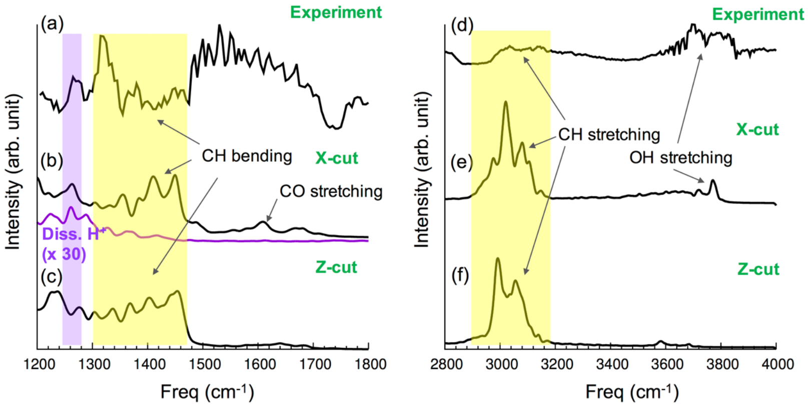

Figure 7. SFG (a,d) and computed vibrational spectra (b,c,e,f) of C−S−H/polymer composites at low (a−c) and high (d−f) frequencies. Computational results obtained with an interface layer thickness of 8 Å for *X*-cut and *Z*-cut systems without water above CSH; see S4 of the Supporting Information for more details. The experimental SFG vibrational spectra are taken in SSP polarizations.

penetrates into the interfacial region between the polymer and the cement.

Spectroscopic Properties. In light of the bonding picture presented above, we proceed to compute the vibrational spectra of C−S−H/polymer interactions that can provide easily identifiable signatures revealing the local bonding motifs. Vibrational spectra can be extracted from the autocorrelation of the atomic velocities obtained from the AIMD trajectories from the formula

$$I(\omega) = \int_0^\infty \mathrm{d}t \frac{\langle v(0)v(t)\rangle}{\langle v(0)v(0)\rangle} \cos(\omega t)$$

where $I(\omega)$ is the vibrational density of states obtained from the cosine transform of the velocity ($v(t)$) autocorrelation function and cosine function. The current approach is in the spirit of Khatib and Sulpizi[45] and can be used to compare the peak positions in nonlinear spectroscopies, but care needs to be taken regarding intensities.[46] By considering collective motions of atoms in each functional group, we can assign peaks of the overall spectra to specific vibrational modes.

To validate our theoretical model, SFG measurements were collected from samples specifically prepared to mimic the C−S−H/polymer interface used in the AIMD simulations. Note that direct comparison of the intensity of the spectra from calculations and experiment is not meaningful; however, we can reliably compare the peak positions. Owing to the fact that only atoms at the C−S−H/polymer interface contribute to SFG signals, for our simulations, we only take into account atoms within a given thickness of the interface. A more detailed description is provided in section S4 of the Supporting Information.

In the lower frequency region, as shown in Figure 7a−c, we identify two areas between 1200−1500 and 1500−1800 cm^{-1}. In the *X*-cut case, the band at ∼1270 cm^{-1} is associated to the proton transfer from the polymer OH groups to the C−S−H surface (highlighted in purple on Figure 7) and the CH bending mode(Figure S8a). Experimentally, this peak is only present when there is polymer on the surface; see Figure S7e,f. From the simulations, we can assign the signal due to specific atoms, and we have found that this peak is clearly associated with proton transfer from the polymer OH groups and matches the experimental peak in terms of position, shape, and width. This is also evident in Figure S9 that shows a fast and irreversible proton transfer from the polymer OH to form a surface OH and a Ca-bound alcoxy group. This suggests that in fact the proton transfer events in the samples are more abundant than the lower number events captured by the finite models used in the AIMD simulations. The cluster of bands between 1300 and 1500 cm^{-1} are associated with the CH bending modes of the polymer (yellow). In the *Z*-cut case, only the 1350−1500 cm^{-1} bands are present. From 1500 to 1800 cm^{-1}, the peak intensity arises mainly from the OH bending mode of the water molecules within the C−S−H component and a small contribution by the polymer's CO stretching mode. We note that in the *Z*-cut case, although the CH contributions are also present, the intensity in the 1500−1800 cm^{-1} region is very low owing to the absence of water in the immediate vicinity of the interface.

In the higher frequency regions, as shown in Figure 7d−f, two separate bands are clearly observed, one in the 2900−3100 cm^{-1} range associated to the polymer CH stretch (yellow) and another one in the 3600−3900 cm^{-1} range from the OH stretch. Similarly, to the low frequency case, the *Z*-cut shows much weaker intensities of the OH stretch because of the absence of water near the interface. This is evident in the SFG spectra where both bands are observed, with the *X*-cut being a closer match to the experimental frequencies for the OH stretches in both shape and position. Confirmation of these assignments can also be seen in Figure S7 (Supporting Information), where the comparison with the C−S−H reference is also provided. On this basis, we conclude that the sample preparation method results in a structure that closely mimics the *X*-cut surface model.

CONCLUSIONS

The analysis presented was motivated by recent developments of novel thermally stable self-healing polymer−cement composites and the need to connect molecular properties to function and healing mechanisms. We achieved this by a unique combination of large-scale (ca. $\sim 10^3$ atoms) AIMD simulations and SFG-VS spectroscopy with submonolayer sensitivity. Mechanistic details of such a complicated interface vary with the choice of models and methods. Furthermore, a reactive molecular model was mandatory to describe how the polymer adheres to a cement fracture. Our model predicted that the critical bonding motif at the C−S−H/polymer interface stems from the polymer OH deprotonation and exhibits a unique signature at $\sim$1270 cm^{-1}. It was subsequently validated by the SFG vibrational spectra. As a side remark, the thiol-ether and disulfide groups that contribute to the self-healing within the polymer do not participate in adhesion of the polymer to the surface but in fact are turned away from the interface. We believe that this further contributes to the healing properties of the composites, as these functional groups remain free to heal the polymer when and where needed.

ASSOCIATED CONTENT

Supporting Information

The Supporting Information is available free of charge on the ACS Publications website at DOI: 10.1021/acsami.7b13309.

> Validation of structural models; bond decay time autocorrelation functions; motion of the polymer center of mass; vibrational analyses; motion of the polymer center of mass; and experiments (PDF)

AUTHOR INFORMATION

Corresponding Authors

*E-mail: Carlos.Fernandez@pnnl.gov (C.F.).
*E-mail: Vanda.Glezakou@pnnl.gov (V.-A.G.).

ORCID

Kenton A. Rod: 0000-0003-1818-9094
Carlos Fernandez: 0000-0002-5102-1341
Roger Rousseau: 0000-0003-1947-0478
Vassiliki-Alexandra Glezakou: 0000-0001-6028-7021

Author Contributions

M.-T.N., R.R., and V.-A.G. designed, executed, and analyzed the simulations and wrote the manuscript. Z.W. performed the SFG-VS studies. C.F. proposed the SFG-VS experiments and with P.K.K. co-designed the approach for the SFG sample preparation. K.A.R., M.I.C., and W.D.B. prepared the polymer−cement samples.

Funding

Funding for this research was provided by the Department of Energy's Geothermal Technology Office. Pacific Northwest National Laboratory is operated by Battelle for the U.S. DOE under contract DE-AC06-76RLO 1830.

Notes

The authors declare no competing financial interest.

ACKNOWLEDGMENTS

This research used resources of the National Energy Research Scientific Computing Center, a DOE Office of Science User Facility supported by the Office of Science of the U.S. Department of Energy under Contract no. DE-AC02-05CH11231. The SFG measurements were performed at the William R. Wiley Environmental Molecular Science Laboratory (EMSL), a national scientific user facility sponsored by the U.S. Department of Energy's Office of Biological and Environmental Research. The authors thank Anthony Guzman (EED) for assistance with sample preparation.

ABBREVIATIONS

C−S−H, calcium−silicate−hydrate; PVA, nylon-6, poly(vinyl)-alcohol; AIMD, ab initio molecular dynamics; PMF, potential of the mean force; VACF, velocity autocorrelation function; SFG, sum frequency generation; GGA, generalized gradient approximation; PBE, Perdew−Burke−Ernzerhof; MOLOPT, molecularly optimized

REFERENCES

(1) Monteiro, P. J. M.; Miller, S. A.; Horvath, A. Towards Sustainable Concrete. *Nat. Mater.* **2017**, *16*, 698−699.

(2) Ball, P. Material Witness: Holding Rome Together. *Nat. Mater.* **2015**, *14*, 139.

(3) Balazs, A. C.; Emrick, T.; Russell, T. P. Nanoparticle Polymer Composites: Where Two Small Worlds Meet. *Science* **2006**, *314*, 1107−1110.

(4) Dolado, J. S.; van Breugel, K. Recent Advances in Modeling for Cementitious Materials. *Cem. Concr. Res.* **2011**, *41*, 711−726.

(5) Qomi, M. J. A.; Krakowiak, K. J.; Bauchy, M.; Stewart, K. L.; Shahsavari, R.; Jagannathan, D.; Brommer, D. B.; Baronnet, A.; Buehler, M. J.; Yip, S.; Ulm, F.-J.; Van Vliet, K. J.; Pellenq, R. J.-M. Combinatorial Molecular Optimization of Cement Hydrates. *Nat. Commun.* **2014**, *5*, 4960.

(6) Pellenq, R. J.-M.; Kushima, A.; Shahsavari, R.; Van Vliet, K. J.; Buehler, M. J.; Yip, S.; Ulm, F.-J. A Realistic Molecular Model of Cement Hydrates. *Proc. Natl. Acad. Sci. U.S.A.* **2009**, *106*, 16102−16107.

(7) Ulm, F.-J. Innovationspotenzial Beton: Von Atomen Zur Grünen Infrastruktur. *Beton- Stahlbetonbau* **2012**, *107*, 504−509.

(8) Matsuyama, H.; Young, J. F. Intercalation of Polymers in Calcium Silicate Hydrate: A New Synthetic Approach to Biocomposites? *Chem. Mater.* **1999**, *11*, 16−19.

(9) Matsuyama, H.; Young, J. F. Synthesis of Calcium Silicate Hydrate/Polymer Complexes: Part Ii. Cationic Polymers and Complex

Formation with Different Polymers. *J. Mater. Res.* **1999**, *14*, 3389−3396.

(10) Ray, S. S.; Okamoto, M. Polymer/Layered Silicate Nanocomposites: A Review from Preparation to Processing. *Prog. Polym. Sci.* **2003**, *28*, 1539−1641.

(11) Mojumdar, S. C.; Raki, L. Preparation and Properties of Calcium Silicate Hydrate-Poly(Vinyl Alcohol) Nanocomposite Materials. *J. Therm. Anal. Calorim.* **2005**, *82*, 89−95.

(12) Mojumdar, S. C.; Raki, L. Preparation, Thermal, Spectral and Microscopic Studies of Calcium Silicate Hydrate−Poly(Acrylic Acid) Nanocomposite Materials. *J. Therm. Anal. Calorim.* **2006**, *85*, 99−105.

(13) Franceschini, A.; Abramson, S.; Mancini, V.; Bresson, B.; Chassenieux, C.; Lequeux, N. New Covalent Bonded Polymer−Calcium Silicate Hydrate Composites. *J. Mater. Chem.* **2007**, *17*, 913−922.

(14) Ioannidou, K.; Kanduč, M.; Li, L.; Frenkel, D.; Dobnikar, J.; Del Gado, E. The Crucial Effect of Early-Stage Gelation on the Mechanical Properties of Cement Hydrates. *Nat. Commun.* **2016**, *7*, 12106.

(15) Shalchy, F.; Rahbar, N. Nanostructural Characteristics and Interfacial Properties of Polymer Fibers in Cement Matrix. *ACS Appl. Mater. Interfaces* **2015**, *7*, 17278−17286.

(16) Sakhavand, N.; Muthuramalingam, P.; Shahsavari, R. Toughness Governs the Rupture of the Interfacial H-Bond Assemblies at a Critical Length Scale in Hybrid Materials. *Langmuir* **2013**, *29*, 8154−8163.

(17) *Well Cementing*, 2nd ed.; Nelson, E. B., Guillot, D., Ed.; Schlumberger: Sugar Land, TX, 2006.

(18) Wu, M.; Johannesson, B.; Geiker, M. A Review: Self-Healing in Cementitious Materials and Engineered Cementitious Composite as a Self-Healing Material. *Constr. Build. Mater.* **2012**, *28*, 571−583.

(19) Van Tittelboom, K.; De Belie, N. Self-Healing in Cementitious Materials—a Review. *Materials* **2013**, *6*, 2182−2217.

(20) Childers, M. I.; Nguyen, M.-T.; Rod, K. A.; Koech, P. K.; Um, W.; Chun, J.; Glezakou, V.-A.; Linn, D.; Roosendaal, T. J.; Wietsma, T. W.; Huerta, N. J.; Kutchko, B. G.; Fernandez, C. A. Polymer-Cement Composites with Self-Healing Ability for Geothermal and Fossil Energy Applications. *Chem. Mater.* **2017**, *29*, 4708−4718.

(21) Perdew, J. P.; Burke, K.; Ernzerhof, M. Generalized Gradient Approximation Made Simple. *Phys. Rev. Lett.* **1996**, *77*, 3865−3868.

(22) Perdew, J. P.; Ruzsinszky, A.; Csonka, G. I.; Vydrov, O. A.; Scuseria, G. E.; Constantin, L. A.; Zhou, X.; Burke, K. Restoring the Density-Gradient Expansion for Exchange in Solids and Surfaces. *Phys. Rev. Lett.* **2008**, *100*, 136406.

(23) Zhang, Y.; Yang, W. Comment on Generalized Gradient Approximation Made Simple. *Phys. Rev. Lett.* **1998**, *80*, 890.

(24) VandeVondele, J.; Krack, M.; Mohamed, F.; Parrinello, M.; Chassaing, T.; Hutter, J. Quickstep: Fast and Accurate Density Functional Calculations Using a Mixed Gaussian and Plane Waves Approach. *Comput. Phys. Commun.* **2005**, *167*, 103−128.

(25) Grimme, S. Semiempirical Gga-Type Density Functional Constructed with a Long-Range Dispersion Correction. *J. Comput. Chem.* **2006**, *27*, 1787−1799.

(26) Lippert, G.; Hutter, J.; Parrinello, M. A Hybrid Gaussian and Plane Wave Density Functional Scheme. *Mol. Phys.* **1997**, *92*, 477−487.

(27) VandeVondele, J.; Hutter, J. Gaussian Basis Sets for Accurate Calculations on Molecular Systems in Gas and Condensed Phases. *J. Chem. Phys.* **2007**, *127*, 114105.

(28) Goedecker, S.; Teter, M.; Hutter, J. Separable Dual-Space Gaussian Pseudopotentials. *Phys. Rev. B* **1996**, *54*, 1703−1710.

(29) Verlet, L. Computer "Experiments" on Classical Fluids. I. Thermodynamical Properties of Lennard-Jones Molecules. *Phys. Rev.* **1967**, *159*, 98−103.

(30) Zhang, X.; Chang, W.; Zhang, T.; Ong, C. K. Nanostructure of Calcium Silicate Hydrate Gels in Cement Paste. *J. Am. Ceram. Soc.* **2000**, *83*, 2600−2604.

(31) Kovačević, G.; Persson, B.; Nicoleau, L.; Nonat, A.; Veryazov, V. Atomistic Modeling of Crystal Structure of Ca1.67sihx. *Cem. Concr. Res.* **2015**, *67*, 197−203.

(32) Allen, A. J.; Thomas, J. J.; Jennings, H. M. Composition and Density of Nanoscale Calcium−Silicate−Hydrate in Cement. *Nat. Mater.* **2007**, *6*, 311−316.

(33) Nonat, A. The Structure and Stoichiometry of C-S-H. *Cem. Concr. Res.* **2004**, *34*, 1521−1528.

(34) Youssef, M.; Pellenq, R. J.-M.; Yildiz, B. Glassy Nature of Water in an Ultraconfining Disordered Material: The Case of Calcium−Silicate−Hydrate. *J. Am. Chem. Soc.* **2011**, *133*, 2499−2510.

(35) O'Brien, D. B.; Massari, A. M. Modeling Multilayer Thin Film Interference Effects in Interface-Specific Coherent Nonlinear Optical Spectroscopies. *J. Opt. Soc. Am. B* **2013**, *30*, 1503−1512.

(36) O'Brien, D. B.; Massari, A. M. Experimental Evidence for an Optical Interference Model for Vibrational Sum Frequency Generation on Multilayer Organic Thin Film Systems. Ii. Consideration for Higher Order Terms. *J. Chem. Phys.* **2015**, *142*, 024704.

(37) Li, G.; Dhinojwala, A.; Yeganeh, M. S. Interference Effect from Buried Interfaces Investigated by Angular-Dependent Infrared−Visible Sum Frequency Generation Technique. *J. Phys. Chem. C* **2011**, *115*, 7554−7561.

(38) Sekkal, W.; Zaoui, A.; Benzerzour, M.; Abriak, N. Role of Porosity on the Stiffness and Stability of (001) Surface of the Nanogranular C−S−H Gel. *Cem. Concr. Res.* **2016**, *87*, 45−52.

(39) Galmarini, S.; Aimable, A.; Ruffray, N.; Bowen, P. Changes in Portlandite Morphology with Solvent Composition: Atomistic Simulations and Experiment. *Cem. Concr. Res.* **2011**, *41*, 1330−1338.

(40) Lequeux, N.; Morau, A.; Philippot, S.; Boch, P. Extended X-Ray Absorption Fine Structure Investigation of Calcium Silicate Hydrates. *J. Am. Ceram. Soc.* **1999**, *82*, 1299−1306.

(41) Faucon, P.; Delaye, J. M.; Virlet, J.; Jacquinot, J. F.; Adenot, F. Study of the Structural Properties of the CSH(I) by Molecular Dynamics Simulation. *Cem. Concr. Res.* **1997**, *27*, 1581−1590.

(42) Renaudin, G.; Russias, J.; Leroux, F.; Frizon, F.; Cau-Dit-Coumes, C. Structural Characterization of C−S−H and C−a−S−H Samples—Part I: Long-Range Order Investigated by Rietveld Analyses. *J. Solid State Chem.* **2009**, *182*, 3312−3319.

(43) Childers, M. I.; Nguyen, M.-T.; Rod, K. A.; Koech, P. K.; Um, W.; Chun, J.; Glezakou, V.-A.; Linn, D.; Roosendaal, T. J.; Wietsma, T. W.; Huerta, N. J.; Kutchko, B. G.; Fernandez, C. A. Polymer-Cement Composites with Self-Healing Ability for Geothermal and Fossil Energy Applications. *Chem. Mater.* **2017**, *29*, 4708−4718.

(44) Kumar, R.; Schmidt, J. R.; Skinner, J. L. Hydrogen Bonding Definitions and Dynamics in Liquid Water. *J. Chem. Phys.* **2007**, *126*, 204107.

(45) Khatib, R.; Sulpizi, M. Sum Frequency Generation Spectra from Velocity−Velocity Correlation Functions. *J. Phys. Chem. Lett.* **2017**, *8*, 1310−1314.

(46) Ishiyama, T.; Morita, A. Computational Analysis of Vibrational Sum Frequency Generation Spectroscopy. *Annu. Rev. Phys. Chem.* **2017**, *68*, 355−377.

■ NOTE ADDED AFTER ASAP PUBLICATION

This paper was published on the Web on January 12, 2018, with a minor error in Figure 7a. The corrected version was reposted on January 24, 2018.